

Non-standard cosmic expansion histories: Neutrino decoupling and primordial nucleosynthesis signatures

D. Aristizabal Sierra,^{1,*} S. Gariazzo,^{2,3,†} and A. Villanueva^{4,‡}

¹*Universidad Técnica Federico Santa María - Departamento de Física
Casilla 110-V, Avda. España 1680, Valparaíso, Chile*

²*Istituto Nazionale di Fisica Nucleare (INFN), Sezione di Torino, Via P. Giuria 1, I-10125 Turin, Italy*

³*Instituto de Física Teórica, CSIC-UAM C/ Nicolás Cabrera 13-15, Campus de Cantoblanco UAM, 28049 Madrid, Spain*

⁴*Instituto de Física, Pontificia Universidad Católica de Valparaíso (PUCV), Avda. Brasil 2950, Casilla 4059, Valparaíso, Chile*

Cosmological scenarios with a non-standard equation of state can involve ultrastiff fluids, understood as primordial fluids for which $p/\rho > 1$. Their energy densities can dominate the Universe energy budget at early times, in the otherwise radiation dominated epoch. During that period the Universe undergoes a faster expansion, that has implications for any decoupling process that takes place in that era. Quintessence models or Ekpyrotic cosmologies are good examples of such scenarios. Assuming the ultrastiff state to be thermally decoupled at very early times, if ever coupled, its observational imprints are left solely in the Universe expansion rate and in the radiation energy density. We consider a complete set of ultrastiff fluids and study their signatures in the neutrino decoupling and BBN eras. Measurements of N_{eff} alone place mild constraints on these scenarios, with forthcoming measurements from the Simons Observatory in the Chilean Atacama desert being able to test regions where still sizable effects are observable. However, when BBN data is taken into account, those regions are proven to be barely reconcilable with primordial helium-4 and deuterium abundances measurements. Our findings show that measurements of the primordial helium-4 abundance imply the tightest constraints, with measurements of primordial deuterium being—to a certain extent—competitive as well. We point out that a $\sim 60\%$ improvement on the statistical uncertainty of the primordial helium-4 abundance measurement, will test these scenarios in the region where they can produce sizable effects. Beyond that precision the regions that are accessible degenerate with standard expectations. In that case, although potentially present, neither neutrino decoupling nor BBN observables will be sensitive probes.

CONTENTS

References

12

I. Introduction	1
II. Parametrization of ultrastiff components and non-standard expansion rate	2
III. Neutrino decoupling	3
A. Neutrino decoupling in an ultrastiff dominated cosmological era	4
IV. Primordial nucleosynthesis signatures	6
A. Building the light elements abundances: Standard scenario	7
B. Building the light elements abundances in non-standard scenarios	8
V. Conclusions	10
A. Relevant thermodynamic quantities and collision terms	12
B. Proton leading-order rate in the infinite mass nucleon limit	12
Acknowledgments	12

I. INTRODUCTION

Measurements of light elements abundances along with CMB power spectra provide the most early picture of the primordial Universe we have so far. CMB power spectra strongly supports the Λ CDM model, while at the same time placing tight constraints on possible new effects at temperatures of the order of 1 eV [1]. Meanwhile Big Bang Nucleosynthesis (BBN), triggered—roughly—when the average photon distribution energy reaches values that allow light nuclei binding, embody the most ancient prove of the physics that took place much before the formation of the large-scale structure of the Universe. It furnishes a powerful tool that enables testing physics beyond the Λ CDM model at temperatures of the order of 0.1 MeV [2]. In the future, measurements of earlier epochs observables such as those from the cosmic neutrino background or from gravitational waves will provide a picture dating back to times where the primordial plasma was at much higher temperatures [3–8].

Deviations from the Λ CDM model can be induced by a variety of new physics scenarios. However, given the excellent match between observational data and Λ CDM predictions, they are expected to be small at least up to the BBN era. From the microphysics point of view, quite generically, the deviations can be categorized as being generated by: (i) New degrees of freedom (particle physics), (ii) changes on the dynamics of the Universe expansion rate (gravity, fluid composition), (iii) combinations of (i) and (ii). This is some-

* daristizabal@ulg.ac.be

† stefano.gariazzo@ift.csic.es

‡ angelodav@gmail.com

what expected. Densities of whatever kind are tracked with kinetic equations which involve information on particle and expansion dynamics. At the MeV scale imprints can be left in two main observables, N_{eff} (measured at either the BBN or CMB era) and/or the relative abundance of light elements in particular those of deuterium and helium-4. With N_{eff} determined at the ten-percent level [1, 9–11] and the deuterium and helium-4 abundances at the percent level [12, 13], constraints arising from early Universe physics are quite often even more stringent than those derived from laboratory experiments (see e.g. [14]).

A rather representative example of scenarios (i) is that of a light thermal relic¹. Its presence in the early Universe contributes to the radiation density and thus generates deviations on N_{eff} and on primordial abundances [14, 18]. In category (ii) scenarios one could certainly mention scalar-tensor theories [19–21], in particular those realizations with an attractor mechanism towards general relativity [22]. Their main phenomenological effect is that of driving the Universe into a period of non-standard expansion, which ultimately at the time of BBN converges towards that predicted by the standard cosmological model.

An interesting possibility, beyond these two benchmark cases, is that of an energy density following from a non-standard equation of state. Possible theoretical scenarios that can lead to such contribution include quintessence models [23, 24], Ekpyrotic cosmologies [25, 26] or models with a *stiff matter* component [27, 28]². In the latter case, the equation of state is given by $p_s = \rho_s$ ($\omega_s = 1$) resulting in an energy density component scaling as a^{-6} . Consequently, there is a period during which—in the otherwise radiation dominated epoch—the Universe becomes dominated by the ultra-stiff component (in this particular case called *stiff matter*). Since $\rho_{\text{rad}}^{\text{stand}} < \rho_{\text{rad}}^{\text{non-stand}}$, during that epoch the Universe is expected to expand at a faster rate, thus leading to effects that involve dark matter freeze-out and freeze-in [30, 31] and production of light elements during the BBN epoch [32].

Studying non-standard expansion histories stands by its own. Regardless of whether or not a certain equation of state fits within a compelling theoretical framework, from a phenomenological perspective, it is desirable to identify observational imprints that such “exotic” contributions might have left in cosmological observables. The impact of such contribution in the radiation dominated era is two-fold³: First of all, the energy density of such background will unavoidably contribute to the relativistic degrees of freedom N_{eff} , whose value is fixed at the time of neutrino decoupling. This calls for an analysis

of neutrino decoupling dynamics in the presence of such new energy density. Secondly, since the expansion is affected so will the formation of light elements abundances. This, in turn, calls for an analysis of BBN dynamics. This is what this paper aims at.

As far as we know, implications of stiff matter on the generation of light elements during the BBN era was first investigated in Ref. [32]. Implications of a stiff fluid—as well as of other kind of components—for dark matter freeze-out and freeze-in have been comprehensively considered in Refs. [30, 31]. Using N_{eff} at the time of BBN (taken to be 1 MeV), this reference has determined as well the constraints that these type of scenarios should obey. More recently, constraints from BBN as well as from CMB have been derived for axion kination in Ref. [34]. Here we extend upon the analyses of these references by: (i) Considering the full process of neutrino decoupling with the corresponding network of kinetic equations, (ii) studying BBN with state-of-the-art numerical tools in cases beyond the stiff matter scenario.

Considering neutrino decoupling seems mandatory. With a faster expansion rate the evolution of the photon and neutrino densities (temperatures) are expected to change. The exotic component will have, therefore, a two-fold effect on N_{eff} : Through its change on T_γ/T_ν and through its direct contribution to the radiation density. The neutrino decoupling process is also relevant since it determines the temperature at which entropy release from e^+e^- pair annihilation ceases, required for a proper evaluation of N_{eff} . For the same reason that neutrino decoupling should be considered, a precise determination of constraints in parameter space implied by BBN calls for a detailed tracking of light elements densities. A faster expansion rate is expected to accelerate electroweak processes decoupling. The neutron-to-proton ratio is then expected to depart from its standard expectation, thus affecting—potentially sizably—the ^4He abundance along with the other abundances.

The remainder of this paper is organized as follows. In Sec. II, we briefly discuss our notation and the parametrization that allows a model-independent treatment of the ultrastiff components. In Sec. III, after discussing the current status of measurements of N_{eff} and future improvements, we present our analysis of neutrino decoupling in these kind of scenarios. Sec. IV discusses the generation of the light elements abundances, along with a short review of the status of the measurements of primordial deuterium and helium-4 abundances. Finally, in Sec. V we conclude and present our summary. In App. A and B a few relevant standard results are given.

II. PARAMETRIZATION OF ULTRASTIFF COMPONENTS AND NON-STANDARD EXPANSION RATE

Phenomenological consequences of ultrastiff fluids can be derived by using a simple—yet powerful—model-independent parametrization first introduced, as far as we know, in Ref. [30]. Since our analyses rely heavily on that parametrization here we briefly review its main aspects. Pressure and energy density can always be related through the sim-

¹ MeV reheating scenarios are as well a rather representative example, see e.g. Refs. [15–17].

² Note that although possible, construction of stiff fluid cosmological models is challenging [29].

³ Here we emphasize on imprints potentially left on observables already measured. There are of course other imprints one can think about. For instance, deviations on dark matter decoupling [30, 31] or effects on the generation of the cosmic baryon asymmetry through leptogenesis. The latter has been already considered, but in a different class of non-standard expansion history scenarios (scalar-tensor theories) [33].

ple equation of state $p = \omega\rho$. For a time-independent proportionality constant, integration of the fluid equation leads to $\rho = \rho_0 a^{-3(1+\omega)}$ ($\rho_0 = \text{const}$). Matter, radiation and vacuum energy densities are characterized by $\omega_{\text{mat}} = 0$, $\omega_{\text{rad}} = 1/3$ and $\omega_{\Lambda} = -1$. As previously pointed out, the case of stiff matter is defined by $\omega = 1$. Barring the case $\omega = 2/3$, all the other scenarios are defined by $\omega > 1$, which include the case of Ekpyrotic cosmologies. Note that ultrastiff fluids are defined by the condition $p/\rho > 1$ (see e.g. [35]), we include—however— $\omega = 2/3$ and $\omega = 1$ in that definition.

In order to compare with radiation it proves useful to introduce

$$\rho_s(a) = \rho(a_c) \left(\frac{a_c}{a}\right)^{4+n}, \quad (1)$$

where a_c is the value of the scale factor at crossover time, when ρ_{rad} and ρ_s match. From now on we will refer to that epoch as the *ultrastiff-radiation equality era*. Departures from standard radiation, as those we are interested in, require $n > 1$ with $\omega = (1+n)/3$. Since we are interested in tracking densities with kinetic equations it proves convenient to rewrite Eq. (1) in terms of temperature. Conservation of entropy per comoving volume, $g_{*S}(T) a^3 T^3 = \text{const}$, enables that. The result reads

$$\rho_s(T_\gamma, T_c, n) = \rho_s(T_c) \left[\frac{g_{*S}(T_\gamma)}{g_{*S}(T_c)} \right]^{(4+n)/3} \left(\frac{T_\gamma}{T_c} \right)^{4+n}. \quad (2)$$

Here T_c refers to the temperature of the heat bath at ultrastiff-radiation equality and n determines the stiffness of the ultrastiff fluid. Note that in the temperature range we are interested in, $T_\gamma \in [10^{-2}, 10]$ MeV, $g_{*S}(T_\gamma)$ has a temperature dependence determined by the photon overheating implied by electron-positron annihilation after neutrino decoupling. Note that $\rho_s(T_c) = \rho_{\text{rad}}(T_c)$, where $\rho_{\text{rad}}(T_c)$ is the standard expression for radiation

$$\rho_{\text{rad}}(T_\gamma) = \frac{\pi^2}{30} g_{*}(T_\gamma) T_\gamma^4, \quad (3)$$

evaluated at the crossover temperature. The energy budget thus follows from

$$\rho_{\text{Tot}}(T_\gamma, T_c, n) = \rho_{\text{rad}}(T_\gamma) + \rho_s(T_\gamma, T_c, n). \quad (4)$$

The amount of energy density in the heat bath is now a parameter-dependent quantity and so the expansion rate

$$H(T_\gamma, T_c, n) = \sqrt{\frac{8\pi}{3m_{\text{Pl}}^2} \rho_{\text{Tot}}(T_\gamma, T_c, n)}. \quad (5)$$

From Eqs. (4) and (5) it becomes clear that imprints of the ultrastiff fluid are left in the amount of extra radiation as well as in the expansion rate. The latter has—of course—ramifications in any decoupling process occurring in the heat bath at the time when the contribution of the ultrastiff fluid is still relevant.

In the setups we are considering the ultrastiff fluid is assumed to have gone through decoupling, if ever thermally

coupled, at very early times. Thus, it has no implications whatsoever in the microphysical processes taking place in the heat bath. The evolution of ρ_s is dictated by a collisionless Boltzmann equation. The collision terms in the network of Boltzmann equations we employ in the next sections are thus unaffected by the presence of the ultrastiff fluid.

III. NEUTRINO DECOUPLING

During the neutrino decoupling era the presence of an ultrastiff fluid is expected to affect, potentially sizably, N_{eff} (the amount of radiation beyond photons). The most obvious way is by its direct contribution to the bulk of the radiation energy density. The none so obvious way, however, is through the impact on the expansion rate. Modification of the expansion rate at this epoch is expected to have an impact on the evolution of both the neutrino and photon temperatures, T_ν and $T \equiv T_\gamma$.

A simplified picture of neutrino decoupling in the standard model is as follows. At temperatures of the order of 10 MeV, species are in thermal contact through electroweak interactions⁴. Because of the low temperature, the most abundant species are e^\pm pairs, photons and the three neutrino flavors, which at this epoch are still relativistic. Densities for all the other species are Boltzmann suppressed and so have a negligible effect (the exception being nucleons which, despite their small densities, become relevant afterwards as their densities feed the formation of the light elements at $T \simeq 0.1$ MeV, see Sec. IV). As the temperature decreases, neutrino-electron electroweak scattering processes slow down (compared with the expansion rate), and so at $T \simeq 1$ MeV neutrinos decouple from the thermal bath. Soon after neutrino decoupling—at $T \lesssim m_e$ —electron-positron pair production becomes inefficient (because of kinematic reasons), thus favoring entropy injection to the hot plasma. The photon thermal distribution gets overheated, but not the neutrino distributions which are already decoupled. The number of relativistic degrees of freedom during this epoch, along with entropy conservation leads to $T_\nu/T = (4/11)^{1/3}$ (see [36] for a detailed discussion).

In the standard model, during the radiation dominated epoch, neutrinos fix the expansion rate. The amount of radiation at the end of the neutrino decoupling era can be parameterized according to [37, 38]

$$\rho_{\text{rad}} = \left[1 + \frac{7}{8} \left(\frac{4}{11} \right)^{4/3} N_{\text{eff}} \right] \rho_\gamma, \quad (6)$$

from which an expression for N_{eff} follows

$$N_{\text{eff}} = \frac{8}{7} \left(\frac{11}{4} \right)^{4/3} \left(\frac{\rho_{\text{rad}} - \rho_\gamma}{\rho_\gamma} \right). \quad (7)$$

In this way N_{eff} parametrizes not only the neutrino contribution to the radiation energy density, but all other radiation

⁴ Through electromagnetic interactions as well, but these are irrelevant for neutrino decoupling.

components, if any. Assuming that only neutrinos and photons are present and that their temperatures suffice to specify their distributions, the leading order standard model expectation is $N_{\text{eff}} = 3$. Subleading effects including QED thermal corrections, neutrino flavor oscillations and a full assessment of the neutrino-neutrino collision integral have been studied in Refs. [39–42]. With these corrections accounted for the standard model value is given by [40] (see also Refs. [41, 43])

$$N_{\text{eff}}^{\text{SM}} = 3.0440 \pm 0.0002, \quad (8)$$

where uncertainties are dominated by numerics and measurements of the solar neutrino mixing angle. Results from a more recent analysis in Ref. [44] are inline with those in Eq. (8).

Observationally, values for N_{eff} follow either from CMB or BBN data sets. Using Planck satellite data, fits of the standard cosmological model lead to [1]

$$N_{\text{eff}}^{\text{CMB}} = 2.99 \pm 0.17 \quad (68\% \text{ CL}), \quad (9)$$

whereas values inferred from primordial nucleosynthesis are

$$N_{\text{eff}} = \left(\frac{11}{4}\right)^{4/3} \left\{ 3 \left(\frac{T_V}{T}\right)^4 + \frac{4 g_*(T_c)}{7} \left[\frac{g_{*S}(T)}{g_{*S}(T_c)} \right]^{(4+n)/3} \left(\frac{T}{T_c}\right)^n \right\}. \quad (11)$$

As expected, this result converges to the standard case in the absence of the ultrastiff contribution component. From this expression it becomes clear that variations on N_{eff} can be due to variations on T and T_V (implied by a faster expansion rate), by the ultrastiff component itself or more generally by both. To determine the extent at which the photon and neutrino temperature changes because of a faster expansion rate we rely on a simplified, yet precise, set of Boltzmann equations: Relevant species are assumed to follow thermal equilibrium distributions, thermally-averaged cross sections assume Maxwell-Boltzmann distributions, the electron mass in the collision terms as well as chemical potentials are neglected. The simplified system of Boltzmann equations reads [49, 50]

$$\frac{dT_V}{dt} = -HT_V + \frac{\delta\rho_{\nu_e} + 2\frac{\delta\rho_{\nu_\mu}}{\delta t}}{3\frac{\partial\rho_\nu}{\partial T_V}}, \quad (12)$$

$$\frac{dT}{dt} = -\frac{4H\rho_\gamma + 3H(\rho_e + p_e) + \frac{\delta\rho_{\nu_e}}{\delta t} + 2\frac{\delta\rho_{\nu_\mu}}{\delta t}}{\frac{\partial\rho_\gamma}{\partial T} + \frac{\partial\rho_e}{\partial T}}. \quad (13)$$

Here $\delta\rho_{\nu_e}/\delta t$ and $\delta\rho_{\nu_\mu}/\delta t$ refer to collision terms. Their explicit expressions along with expressions for the other relevant thermodynamical quantities are given in Appendix A. Note that the results derived with Eqs. (12) and (13), presented below, have been double-checked with the aid of the FortEPiANO public code [40, 51]. Results in both cases are inline.

We start with the determination of departures of T/T_V from the standard expectation, $T/T_V = 1.3961$ [49]. Considering

instead given by [9–11, 45]

$$N_{\text{eff}}^{\text{BBN}} = 2.843 \pm 0.154 \quad (95\% \text{ CL}). \quad (10)$$

Improvements upon these values are expected from the Simons Observatory in the Chilean Atacama desert (stage-III CMB experiment) [46], which aims at a precision of $\sigma(N_{\text{eff}}) = 0.05$. Further improvements are expected as well from CMB-S4 [47], a follow-up stage-IV CMB experiment, that aims at a precision of $\sigma(N_{\text{eff}}) = 0.03$ [48].

A. Neutrino decoupling in an ultrastiff dominated cosmological era

With the ultrastiff contribution and assuming an universal temperature for the three neutrino flavor species ($T_{\nu_i} = T_V$), Eqs. (2) and (7) allow writing

(as a benchmark scenario) the case $T_c = 0.1 \text{ MeV}$ for four different ultrastiff fluid choices $n = 1, \dots, 4$, we calculated the time evolution of the neutrino and photon temperatures (densities) with the aid of Eqs. (12) and (13). For the determination of the time integration limits we have used the time-temperature Jacobian

$$\left| \frac{dt}{dT} \right| = \frac{1}{H(T, T_c, n) T} \left[1 + \frac{T}{3g_{*S}(T)} \frac{d}{dT} g_{*S}(T) \right], \quad (14)$$

which follows from entropy conservation per comoving volume and which reduces to the standard result $t = 1/2/H(T)$ in the absence of ρ_S and during an epoch of no entropy transfer. Note that the relation between time and temperature is affected because of the ultrastiff contribution. Results are shown in the left graph in Fig. 1.

With increasing n (increasing stiffness), departure from $T_V = T$ starts at earlier times (higher T). A stiffer energy density component implies a faster expansion rate which, in turn, implies processes to be less effective than otherwise (they abandon their thermal behavior at earlier times). Thus, while at sufficiently high temperatures e^+e^- pair production ($\gamma + \gamma \rightarrow e^+ + e^-$) is as likely as annihilation ($e^+ + e^- \rightarrow \gamma + \gamma$), production ceases to be effective at earlier times because of the higher expansion rate. Entropy starts being released in the hot plasma at earlier times and so the earlier the departure from $T = T_V$. The trend is therefore as follows. The stiffer the component, the more overheated the photon distribution is at the end of the e^+e^- pair annihilation era. For the benchmark scenario we are considering here ($T_c = 0.1 \text{ MeV}$) the largest

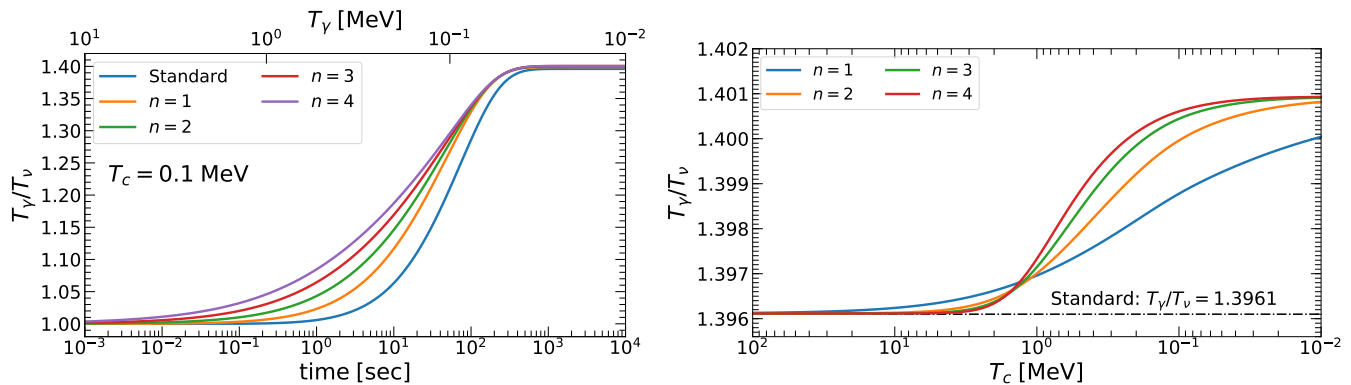


FIG. 1. **Left graph:** T_γ/T_ν ratio as a function of time for different ultrastiff fluid scenarios $n = 1, \dots, 4$ and for a crossover temperature $T_c = 0.1 \text{ MeV}$. The result has been derived by integration of the set of Boltzmann equations in Eqs. (12) and (13). Because of the faster expansion rate, e^+e^- pair annihilation injects entropy to the thermal bath at earlier times. Overheating of the photon distribution temperature changes at the permille level above the standard model expectation. The upper axis, shown just as a guide, displays the temperature calculated assuming $t = 1/2/H$. An accurate expression, used for integration, follows from Eq. (14). **Right graph:** T_γ/T_ν versus crossover temperature T_c for the ultrastiff fluid cases $n = 1, \dots, 4$ (see text for further details). Shown as well is the standard model value without QED finite temperature corrections [49].

departure is found to be ⁵

$$\Delta_4^{\mathcal{W}} = \frac{T/T_\nu|_{n=4} - T/T_\nu|_{\text{Stand}}}{T/T_\nu|_{n=4}} \times 100\% = 0.3\% . \quad (15)$$

To determine the general behavior we have calculated T/T_ν as a function of T_c . Results are shown in the right graph in Fig. 1 for the ultrastiff fluid scenarios $n = 1, \dots, 4$. First of all, one can see that at high T_c values scenarios with small n (less stiff) tend to deviate more from the standard expectation. This behavior can be readily understood from Eq. (2) coupled with results in the left graph of the same figure. From that graph it is clear that e^+e^- pair annihilation ceases at $T \simeq 5 \times 10^{-2} \text{ MeV}$, with small variations about that number depending on n ⁶. Values shown in the right graph in Fig. 1 are those at that value, although integration over time covers values down to $T \simeq 10^{-2} \text{ MeV}$. At large values of T_c , the suppression already implied by a small value of T is further enhanced with increasing values of n . So, the smaller n the larger the deviation in H implied by ρ_s . Conversely, for small values of T_c (comparable to the temperature where e^+e^- pair annihilation ceases) larger values of n produce the largest deviations inline with the result displayed in the graph.

The largest deviations on T/T_ν are found for small T_c and large n , a result somewhat expected. It is for those configurations in parameter space for which one finds the largest deviations on the expansion rate, compared with the standard expansion. For the cases we have considered and up to

$T_c = 10^{-2} \text{ MeV}$, deviations from the standard case are all at the permille level:

$$\Delta_1^{\mathcal{W}} = 0.280\% , \quad \Delta_2^{\mathcal{W}} = 0.336\% , \quad (16)$$

$$\Delta_3^{\mathcal{W}} = 0.342\% , \quad \Delta_4^{\mathcal{W}} = 0.344\% . \quad (17)$$

Increasing n and/or further decreasing T_c will lead to larger deviations. However, those configurations in parameter space are—potentially—not reconcilable with constraints from light elements abundances, in particular with those from ^4He (see Sec. IV). Note that if traces of the ultrastiff fluid were determined only by these deviations, measurements of N_{eff} at the same level of those in Eqs. (16) and (17) would be required to test these scenarios. However, in addition to these deviations, there is as well the contribution of the ultrastiff fluid energy density to N_{eff} that we now discuss.

To determine the effect of ρ_s on N_{eff} we have calculated the second term in Eq. (11) along with the values for T/T_ν determined by Eqs. (12) and (13). Results for N_{eff} as a function of T_c are displayed in the left graph in Fig. 2. The behavior is as follows. N_{eff} converges to its standard value at high T_c . This is somewhat expected, high values of T_c suppress the contribution of ρ_s to N_{eff} and produce an expansion that resembles that of the ΛCDM model. As T_c decreases, both the contribution from ρ_s and the deviations on T/T_ν implied by a faster expansion rate kick in, and so N_{eff} deviates from the standard expectation. The less stiff the contribution to N_{eff} is, the larger the value of T_c where the departure starts growing rapidly. This behavior can be seen in the graph, where sizable deviations are found (as T_c decreases) first for $n = 1$ then for $n = 2$ and so on and so forth.

Using the current 68% CL values for $N_{\text{eff}}^{\text{CMB}}$ in Eq. (9) one finds that consistency with current measurements require—roughly— $T_c \gtrsim \{50.0, 9.00, 5.00, 2.00\} \times 10^{-2} \text{ MeV}$ for $n = \{1, 2, 3, 4\}$. As can be seen in the graph, improvements on N_{eff} measurements—as those expected in stage-III CMB experiments—will be able to explore regions in parameter

⁵ For the percentage relative change in T/T_ν we use the notation $\Delta_i^{\mathcal{W}}$, where i refers to n_i and the difference is calculated with respect to the standard case.

⁶ Recently a detailed calculation of e^+e^- pair annihilation freeze-out, including Fermi blocking and Bose enhancement as well as chemical potentials, has shown that e^+e^- pair annihilation ceases at $T \simeq 16 \text{ keV}$ [52].

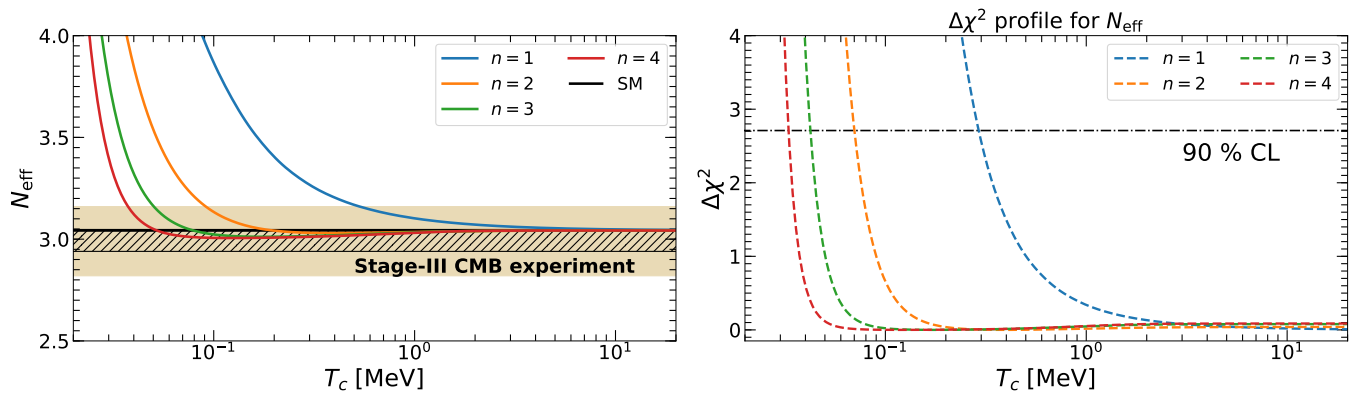


FIG. 2. **Left graph:** N_{eff} as a function of T_c for $n = 1, \dots, 4$. The colored wide stripe corresponds to $N_{\text{eff}}^{\text{CMB}}$ as inferred from Planck data [1] and given in Eq. (9). The hatched region, instead, shows forecast values for N_{eff} , as expected from the Simons Observatory in the Chilean Atacama desert [46]. **Right graph:** $\Delta\chi^2$ profile for the same cases shown in the left graph. The 90% CL upper limits on T_c are shown in Tab. I.

space that so far have not been tested⁷. However, these results have to be coupled with those following from BBN. And, as it will be shown in Sec. IV, those regions are already ruled out by primordial deuterium and helium-4 abundances measurements. Thus, if any deviation from expectation is found in these round of experiments that will further rule out regions of parameter space.

To put these results on a more statistical basis we have performed a χ^2 analysis with the aid of the following least-square function

$$\chi_{\text{CMB}}^2(T_c, n) = \left[\frac{N_{\text{eff}}^{\text{Th}}(T_c, n) - N_{\text{eff}}^{\text{CMB}}}{\sigma(N_{\text{eff}})} \right]^2, \quad (18)$$

where for $\sigma(N_{\text{eff}})$ we employ the statistical uncertainty in Eq. (9). Results are presented in the right graph in Fig. 2. Values for T_c^{min} can be read directly from the graph and are given in Tab. I as a reference. As has been already stressed, these results need to be compared with those derived from the BBN analysis discussed in the following section.

n	1	2	3	4
$T_c^{\text{min}} \times 10^{-2} \text{ MeV}$	29.1	6.98	4.23	3.29

TABLE I. 90% CL lower limit for T_c and for cases $n = 1, \dots, 4$. The results follow after calculating N_{eff} with the aid of Eqs. (11), (12) and (13) and using the χ^2 function given in Eq. (18).

⁷ N_{eff} has been calculated at the temperature at which electron-positron annihilation ceases, which to a large extent amounts to the temperature at which the formation of the light elements abundances freeze-out. For our analysis we have employed, however, $N_{\text{eff}}^{\text{CMB}}$ which matches $N_{\text{eff}}^{\text{BBN}}$ within error bars. Note that here we are assuming that this will be the situation as well with stage-III CMB experiments.

IV. PRIMORDIAL NUCLEOSYNTHESIS SIGNATURES

In this section we determine the impact of ultrastiff fluids on the formation of the light elements abundances. We first start in Sec. IV A with the standard scenario, aiming at a description of the main qualitative features that the generation of the deuterium (d), tritium (t), helium-3 and helium-4 abundances obey. Note that a faster expansion rate is expected—in general—to overproduce all the abundances. This can be readily and qualitatively understood as follows. The neutron-to-proton ratio is expected to deviate from its thermal distribution at higher T . The amount of neutrons available at the onset of BBN is therefore larger and so—in principle—all the light elements yields (see below for a more detailed discussion). Motivated by this we do not consider lithium-7. In the CMB and $D + {}^4\text{He}$ concordance ranges the standard BBN scenario overproduces ${}^7\text{Li}$ [12]. In a faster expanding Universe results are therefore worsen. With the results from Sec. IV A we then proceed to analyze the different non-standard scenarios in Sec. IV B.

Among the light elements abundances those of deuterium and ${}^4\text{He}$ are the better measured. The ideal proxy for primordial deuterium measurements are chemically unprocessed environments, with the most precise determination following from a combination of 16 different measurements from high-redshift and low-metallicity quasar absorption systems using large telescopes [12]:

$$D/H|_p = (25.36 \pm 0.26) \times 10^{-6}. \quad (19)$$

Helium-4 measurements, instead, follow from observations of recombination emission lines of hydrogen and helium in blue compact galaxies (typically at low redshifts). The wealth of data from these sources has allowed a percent determination of the primordial baryon fraction in ${}^4\text{He}$. The latest measurement obtained by combining data from the Sloan Digital Sky Survey (SDSS), blue compact dwarf galaxies [53, 54] and the Primordial Helium Legacy Experiment with Keck (PHLEK) [13] is:

$$Y_p = 0.2436_{-0.0040}^{+0.0039}. \quad (20)$$

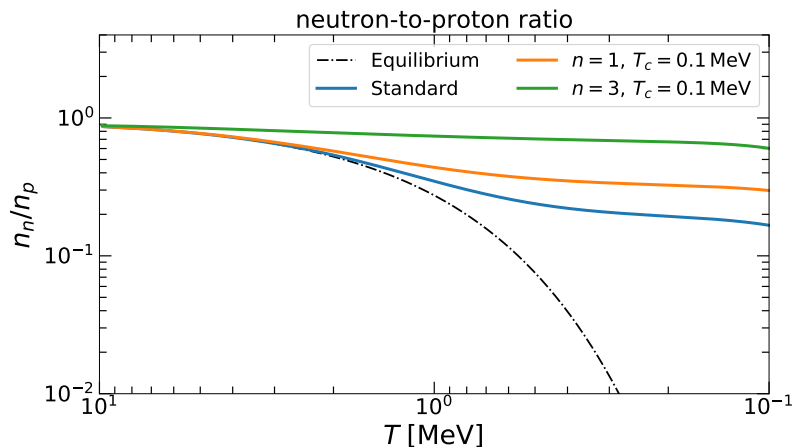


FIG. 3. Neutron-to-proton ratio as a function of temperature in the standard case as well as in the non-standard cases $n = 1$ and $n = 3$ for $T_c = 0.1$ MeV. For comparison, the thermal distribution is also shown. The stiffer the contribution to the energy density is, the higher the temperature at which the neutron-to-proton ratio deviates from its thermal equilibrium distribution. This behavior has an impact on BBN predictions.

Given the precision with which these two quantities are measured, any approach to BBN aiming at reliable predictions should account for higher-order effects. However, a semi-quantitative understanding involving only leading effects is desirable as it captures the main features of the intricate physics taking place during the BBN era. Moreover, it enables a detailed understanding of the effects implied by ultra-stiff fluids. This is what Sec. IV A aims at.

Results presented in this section were obtained with the aid of `PARthENoPE` and a few were double-checked with `PRIMAT` [45, 56–59].

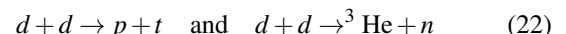
A. Building the light elements abundances: Standard scenario

At temperatures of the order of 10 MeV, neutrons and protons are in thermal contact with the primordial plasma. As the temperature decreases, weak interactions slow down and so the neutron-to-proton ratio deviates from its thermal distribution as can be seen in Fig. 3. The ratio is further suppressed because of neutron decay, which ceases when neutrons become bounded in nuclei. At temperatures of the order of 1 MeV, the most efficient nuclear process is



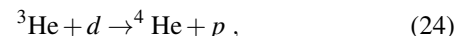
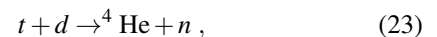
The rate for the production process normalized to the expansion rate is displayed in the top-left graph in Fig. 4. For comparison the helium-3 photon dissociation process ${}^3\text{He} + \gamma \rightarrow p + d$ —magnified by 10^{10} —is displayed as well. At these temperatures forward and backward reactions are taking place at the same rate and so the deuterium abundance building up at this stage is still tiny: Although the temperature of the heat bath is below the deuterium binding energy (2.3 MeV), photon dissociation is still effective enough. The amount of entropy in the plasma is sufficiently large for the high-energy tail of the photon distribution to still entail a large amount

of high-energy photons, capable of breaking down the deuterium binding. As soon as photon dissociation becomes ineffective—at $T \simeq 7 \times 10^{-2}$ MeV—a rapid growth of the deuterium abundance is then triggered (the deuterium abundance reaches its peak), until the deuterium washout processes



kick in at $T \simeq 6 \times 10^{-2}$ MeV (see the top-left graph in Fig. 4). As the temperature decreases below this value, these processes washout the deuterium abundance from its peak at $D/H \simeq 3.65 \times 10^{-3}$ down to its freeze-out value $D/H = 2.51 \times 10^{-5}$ (results for $Y_i = n_i/n_B$ are shown in Fig. 5).

The same processes that washout the deuterium abundance, source the formation of tritium and helium-3. So, as the deuterium abundance grows so does the tritium and helium-3 abundances. And this triggers the growth of helium-4 in the plasma through three (leading) processes:



As can be seen in the top-right graph in Fig. 4, production through tritium annihilation is rather efficient up to $T \simeq 7 \times 10^{-2}$ MeV. Direct production through ${}^3\text{He}$ is instead subdominant, but ${}^3\text{He} - n$ annihilation sources tritium which is then reprocessed into ${}^4\text{He}$. The neutrons left from the process in Eq. (23) enhance the reaction rate. At lower temperatures—of the order of 6×10^{-2} MeV—process (24) becomes relevant and contributes to ${}^4\text{He}$, although at a much lower rate. Right after ${}^4\text{He}$ freezes out a large fraction of neutrons are gone, as they have fueled its formation.

In summary, tritium and ${}^3\text{He}$ source ${}^4\text{He}$ formation, and so their abundance is smaller. Generation of tritium and ${}^3\text{He}$ is sourced by deuterium, which in turn is sourced by neutrons

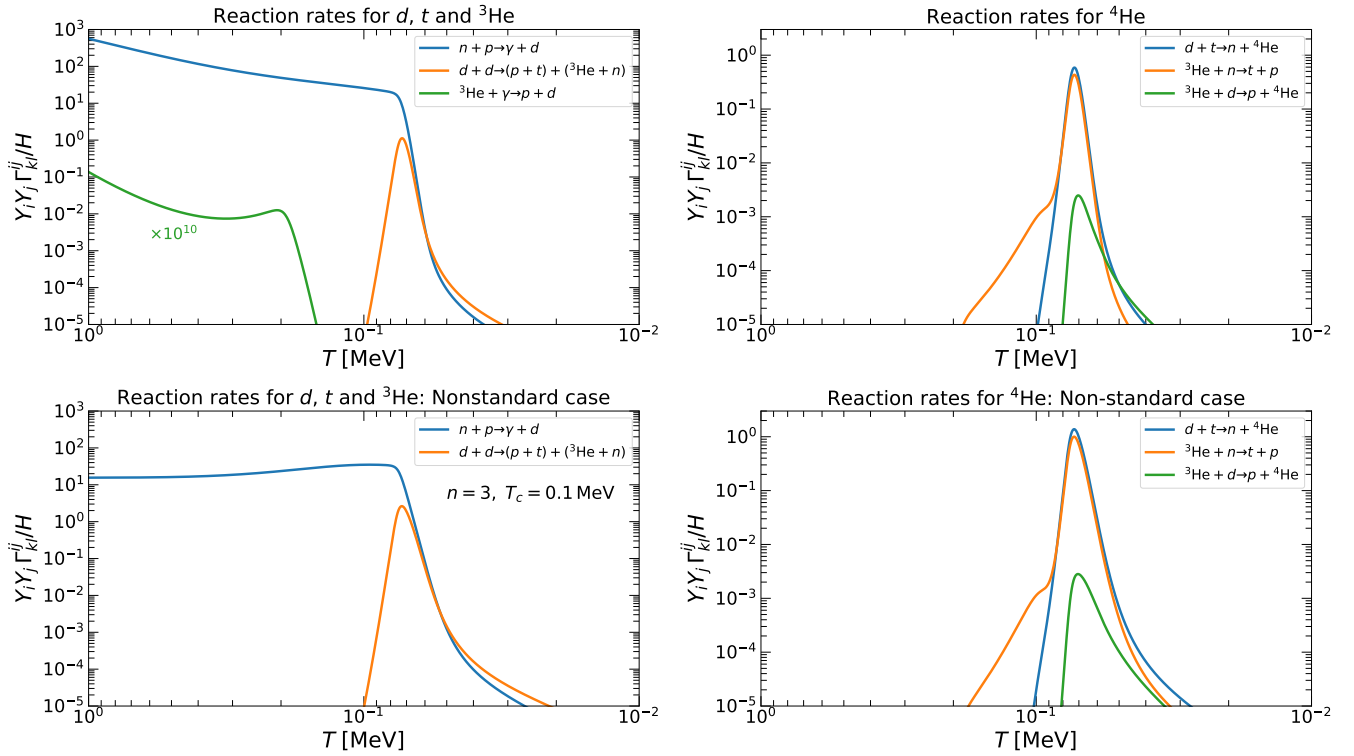


FIG. 4. **Top left:** Most relevant reactions for the generation of the deuterium, tritium and ^3He abundances in the standard scenario. Helium-3 photon dissociation is shown only for comparison. **Top right:** Most relevant processes for the production of ^4He in the standard scenario. **Bottom left:** Same as for the top left graph but for the non-standard case with an ultrastiff background with $n = 3$ and crossover temperature $T_c = 0.1\text{ MeV}$. **Bottom right:** Same as for the top right graph but for the non-standard case with an ultrastiff background with $n = 3$ and crossover temperature $T_c = 0.1\text{ MeV}$. $\Gamma_{kl}^{ij} \equiv \rho_B N_A \langle \sigma v \rangle_{ij \rightarrow kl}$, where $\langle \sigma v \rangle_{ij \rightarrow kl}$ refers to the thermally-averaged cross section for the process $i + j \rightarrow k + l$ and N_A is the Avogadro number. Explicit expressions for this quantity for the different reactions displayed in the graph are taken from [55].

and protons. Along the way deuterium and ^3He washout processes inject protons back into the plasma, but neutrons instead are depleted because ultimately they source all the abundances and more importantly ^4He formation. The amount of neutrons at the onset of BBN thus critically determines its output. The evolution of the different abundances is shown in Fig. 5.

B. Building the light elements abundances in non-standard scenarios

As can be seen in Fig. 3, the neutron-to-proton ratio (number of neutrons and protons available at the onset of BBN) strongly depends on the type of ultrastiff fluid present in that era and on T_c . Lower values of crossover temperature can readily generate, for a sufficiently stiff contribution, a freeze-out neutron-to-proton ratio that exceeds the standard value by more than 75%. With such deviations, and according to the discussion in the previous section, this enhancement can have dramatic consequences on BBN predictions.

A larger neutron-to-proton ratio is expected because of the faster expansion rate. Let us discuss this in more detail. Coupled with the ultrastiff fluid, the modified expansion rate is

steeper than the standard one and so electroweak interactions decouple at higher T ⁸. Equivalently, electroweak interactions happen less often because of the faster expansion and so they undergo freeze-out at earlier times. This is illustrated in Fig. 6, where we have plotted the leading-order proton reaction rate $\Gamma_{p \rightarrow n} \equiv \Gamma_{p+e \rightarrow \bar{\nu}_e+n} + \Gamma_{p+\nu_e \rightarrow \bar{e}+n}$ (see Appendix B for explicit expressions) normalized to the expansion rate as a function of T . Instantaneous neutrino decoupling has been assumed at $T = 1.4\text{ MeV}$. Note that this result is displayed only to illustrate the earlier decoupling induced by the non-standard expansion. Results presented in Figs. 5 along with those in Fig. 7 involve all electroweak decoupling effects included in PARthENoPE.

The most remarkable consequence of electroweak decoupling at higher T is that of increasing the helium-4 abundance. The baryon fraction in helium-4 quoted in Eq. (20) can be well

⁸ Usually, weak freeze-out is quoted to happen at $T \simeq 0.8\text{ MeV}$. However, a proper inclusion of lepton capture on neutrons and protons as well as blocking factors for in-medium free neutron decay has demonstrated that they are still active close to the epoch of ^4He formation ($T \simeq 100\text{ keV}$) [60].

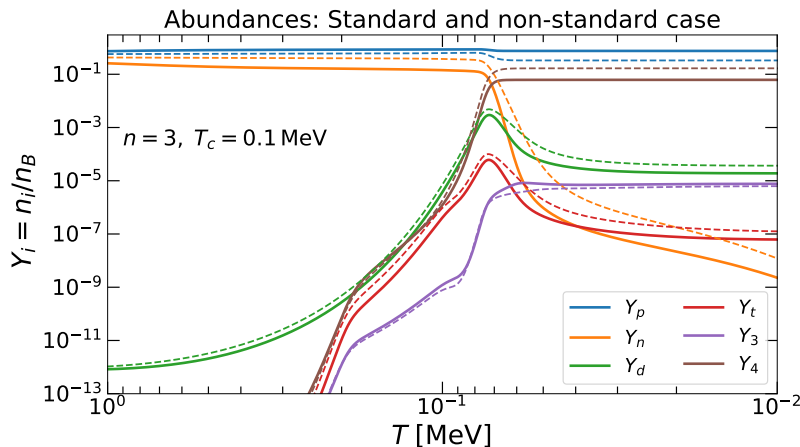


FIG. 5. Evolution of the light elements abundances in the standard scenario as well as in the non-standard scenario $n = 3$ and $T_c = 0.1$ MeV (dashed lines). Results have been derived with `PARthENoPE` [45, 56, 57] properly modified to account for deviations from the standard case. Results follow from $\Omega_B h^2 = 0.023$ and the neutron lifetime fixed to $\tau_n = 885.7$ sec. The latter inline with neutron beam experiments (see text for details). Y_3 and Y_4 refer to the abundances of ^3He and ^4He , respectively.

approximated by

$$Y_p = \frac{2n_n/n_p}{1 + n_n/n_p}, \quad (26)$$

from which it becomes clear that a substantial modification of the neutron-to-proton ratio will, in turn, drastically modify its BBN prediction. Note that in the absence of the ultrastiff fluid, standard case, the n_n/n_p freeze-out temperature is controlled by the neutron lifetime. A larger τ_n means electroweak interactions are weaker, resulting in an earlier decoupling and so in an overproduction of ^4He .

Motivated by a 3.6σ mismatch between neutron beam and ultra-cold neutron (UCN) storage methods measurements [61, 62]

$$\tau_n^{\text{Beam}} = 887.2 \pm 2.2 \text{ sec}, \quad (27)$$

$$\tau_n^{\text{UCN}} = 877.7 \pm 0.7 \text{ sec}, \quad (28)$$

the lifetime of the neutron has been recently a matter of debate. Indeed, the impact of such mismatch has motivated the study of its implications in BBN predictions [63]. Here it is worth stressing that our results demonstrate that deviations on the ^4He abundance—that could be attributed to τ_n —can be as well interpreted/understood in terms of a primordial era dominated by an ultrastiff fluid. The size of the deviation determined by the nature of the fluid (exponent n) and the crossover temperature.

That ^4He is overproduced can be seen directly in Fig. 5, where we have calculated, along with the standard case, results for the case $n = 3$ and $T_c = 0.1$ MeV. This choice, although just a particular case in parameter space, shows the impact of a sufficiently steep energy density contribution. At freeze-out, the standard calculation leads to $Y_p = 0.2469$ while the prediction with an expansion determined by the chosen parameters produces $Y_p = 0.6693$, a number clearly ruled out by data [see Eq. (20)]. From the same Figure one

can as well see that deuterium is also largely overproduced, $D/H|_p = 1.1 \times 10^{-4}$. The number density increases by about a factor of two and the hydrogen (protons) abundance decreases by about the same amount, thus resulting in a $\sim 75\%$ deviation compared with the standard result and ruled out by data [see Eq. (19)]. Tritium follows the same trend, its value increases sizably compared to the standard result. Unlike these elements, helium-3, however, is slightly depleted.

The behavior just described in the previous paragraph can be understood by relying on the leading-order processes governing BBN, and discussed in Sec. IV A for the standard case. Comparing the top and bottom left graphs in Fig. 4 one can see that at the onset of BBN ($T \simeq 0.1$ MeV) deuterium production is more efficient in the non-standard case. This is the case because of the initial-state nucleon density being larger by about a factor of 2. From those graphs one can also note that the processes that populate helium-3 and tritium abundances become effective at slightly lower T , but still enough for the deuterium abundance to reach a higher peak and to decrease less abruptly (see Fig. 5). Since deuterium is more abundant, tritium is more efficiently produced and so its abundance is enhanced. By the same token one would expect the helium-3 abundance to be enhanced, but this is not the case. The reason has to do with the process in Eq. (25). Since neutrons are more abundant, the $^3\text{He} - n$ annihilation rate is higher, resulting in a depletion of its abundance. Note that unlike the standard case $^3\text{He} - d$ annihilation—that will otherwise contribute to deuterium and further helium-3 depletion—is inefficient all across the relevant temperature range.

With the general trend already understood, we are left with the determination of the minimal crossover temperature (T_c^{min}) for which the ultrastiff fluid is still consistent with current $D/H|_p$ and Y_p measurements [see Eqs. (19) and (20)]. For that aim we have calculated these abundances as a function of T_c for different ultrastiff fluid scenarios, $n = 1, \dots, 4$. Results are shown in Fig. 7, top-left (top-right) graph for deuterium

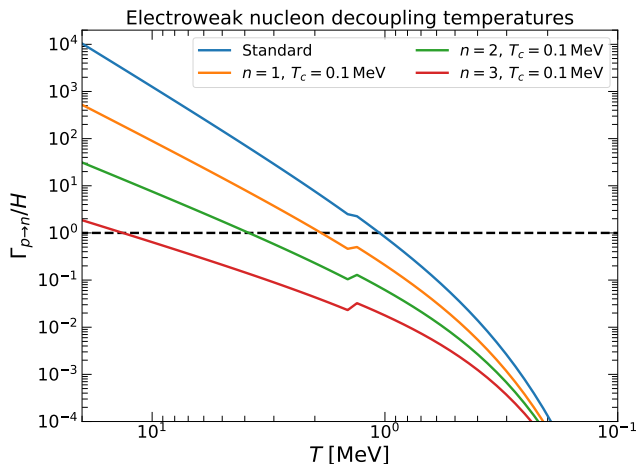


FIG. 6. Leading-order proton electroweak reaction rate $\Gamma_{p \rightarrow n} \equiv \Gamma_{p+e \rightarrow \bar{\nu}_e+n} + \Gamma_{p+\nu_e \rightarrow \bar{e}+n}$ normalized to the expansion rate in the standard case as well as in three different non-standard cases, with $T_c = 0.1$ MeV used as a proxy. It can be seen that non-standard cosmic expansion histories lead to nucleon decoupling at higher temperature.

(${}^4\text{He}$). In line with our previous discussion, ${}^4\text{He}$ places tighter limits on T_c (regardless of the ultrastiff fluid nature). The temperature behavior, however, matches in both cases. The less stiff the background is, the higher the T_c for which consistency with data is found. This is readily understood from the temperature dependence of the ultrastiff fluid energy density [see Eq. (2)]. Because of the boundary condition, ultrastiff-radiation equality is fixed universally regardless of n . At temperatures above T_c , larger values of n produce a broader ρ_s domination epoch. In contrast, below T_c ultrastiff components fade away more abruptly with T . Thus, for small values of n ultrastiff-radiation equality must happen at larger T to prevent the background component to contribute sizably.

Simple inspection of the results indicate that consistency with deuterium data requires $T_c \gtrsim \{8.8, 1.8, 1.2, 1.0\}$ MeV for $n = \{1, 2, 3, 4\}$. For ${}^4\text{He}$, instead, results are $T_c \gtrsim \{32.0, 5.0, 3.0, 2.0\}$ MeV for n covering the same values. To put these results on a more statistical basis we have performed a χ^2 analysis with the aid of the following least-square function

$$\chi_{\text{BBN}}^2(T_c, n) = \left[\frac{\mathcal{A}_{\text{Th}}(T_c, n) - \mathcal{A}_{\text{Exp}}}{\sigma_{\mathcal{A}}} \right]^2, \quad (29)$$

where \mathcal{A} stands for deuterium or ${}^4\text{He}$ abundances and $\sigma_{\mathcal{A}}$ for the statistical uncertainty in Eqs. (19) and (20). Results are shown in Fig. 7 for deuterium (helium-4) in the bottom-left (bottom-right) graph. Values for T_c at the 90% CL are listed in Tab. II. As already mentioned, ${}^4\text{He}$ places the tightest limits, although at this level values are rather comparable to those obtained with deuterium data. Note that values listed in Tab. II are rather inline with those derived in Ref. [30], for arbitrary n . They differ by only 20% – 30%.

In addition to current primordial helium-4 measurements—that imply values in Tab. II—we have considered as well a forecast. To do so, we have set the condition that the statistical uncertainty of such hypothetical measurement allows fully closing the region where the ultrastiff fluid generates a sizable

n	1	2	3	4
$T_c^{\text{min}}(\text{D}/\text{H}_{\text{p}})$ [MeV]	6.660	1.518	1.226	1.154
$T_c^{\text{min}}(Y_{\text{p}})$ [MeV]	11.80	2.838	1.903	1.613

TABLE II. 90% CL lower limit for T_c and for cases $n = 1, \dots, 4$. The results follow after calculating the relative abundance for deuterium and ${}^4\text{He}$ under the presence of the ultrastiff fluid component and with the aid of the χ^2 function in Eq. (29).

departure from the standard expectation. We have found that a measurement reducing the statistical uncertainty by $\sim 60\%$ will test all the relevant values of T_c for which a departure from expectation is observable, at least for the first four realizations $n = 1, \dots, 4$ ($\omega = 2/3, 1, 4/3, 5/3$) of the “full tower”. The hatched region in the top-right graph in Fig. 7 shows the result.

V. CONCLUSIONS

In this paper we have considered the impact of ultrastiff fluids in early Universe dynamics, which emerge in cosmological scenarios with a non-standard equation of state. Since their energy density can dominate at early times they can—potentially—affect the Universe expansion rate and contribute sizably to the amount of “radiation” during that epoch. Given that BBN data provides the most early picture of the early Universe, we have focused our analysis on the possible traces left by this type of backgrounds on neutrino decoupling and BBN observables.

Considering neutrino decoupling seems—to a certain extent—mandatory. First of all, is during this process that the photon distribution temperature gets overheated (above that of the neutrinos). And in a faster expanding Universe that overheating is expected to be affected, mainly because of the impact on the temperature where electron-positron pair annihila-

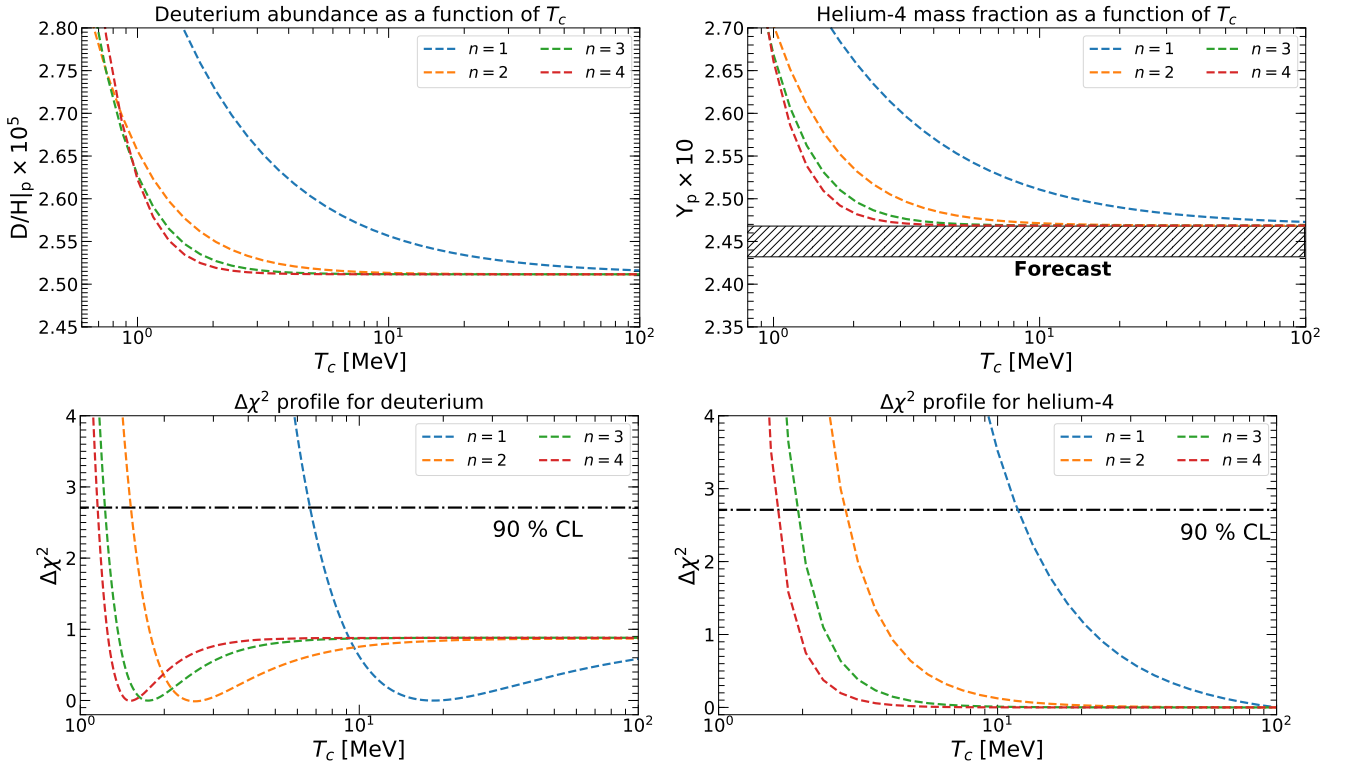


FIG. 7. **Top:** Deuterium (left graph) and helium-4 (right graph) abundances $D/H|_p$ and Y_p as a function of crossover temperature T_c for exponential indices $n = 1, \dots, 4$. The stripes correspond to allowed measured intervals given in Eqs. (19) and (20) and taken from Refs. [12, 13]. The hatched region correspond to a forecast where the statistical uncertainty has been required to close the region where ultrastiff fluids can generate a sizable deviation from the standard expectation. **Bottom:** $\Delta\chi^2$ profiles for deuterium (left graph) and helium (right graph) as a function of T_c . The 90% CL limit on T_c can be directly read from both graphs. The absence of an absolute minimum for $\Delta\chi^2$ in the helium-4 case is due to the theoretical prediction never reaching the measured central value.

tion ceases. An overheating of the photon distribution above standard expectations has consequences on N_{eff} , beyond those already implied by the ultrastiff fluid.

A faster expansion rate is also expected to affect the network of kinetic equations accounting for the formation of the light elements abundances. From a very simplified point of view, the mere fact that the neutron-to-proton ratio can be dramatically changed at the onset of BBN already suggest that light elements abundances are good “tracers” of the imprints left by these fluids.

Our findings are as follows. Neutrino decoupling alone, coupled with indirect measurements of N_{eff} inferred from CMB power spectra, are able to test some regions in the $n - T_c$ plane. Their extent, however, is mild and so allow for crossover temperatures to be as small as 10^{-1} MeV depending on stiffness. Improvements in N_{eff} measurements, as those expected in stage-III or stage-IV CMB experiments, can change that conclusion. If they were to be considered alone, expectations from these forthcoming measurements could improve sensitivities by a factor of a few.

When BBN data is used instead, sensitivities from N_{eff} are proven to be within regions that are hard to reconcile with measurements of primordial helium-4 abundances. Thus, a deviation of N_{eff} from standard expectations cannot be ac-

counted for by this type of early Universe physics. Primordial helium-4 and deuterium measurements, in particular the former, have the largest sensitivities. Less stiff scenarios are more prone to the constraints implied by these data. For $n = 1$, ultrastiff-radiation equality needs to happen above ~ 12 MeV, i.e. much before the onset of neutrino decoupling and BBN. With increasing stiffness ultrastiff-radiation equality can happen at lower temperatures. In the case of stiff matter ($\omega = 1$, $n = 2$) that equality can be as low as 3 MeV, while still being consistent with current primordial helium-4 measurements.

We have shown that improving the statistical uncertainty in the primordial helium-4 abundance measurement by $\sim 60\%$, will increase sensitivities to regions where still these fluids can leave traceable tracks. So, with such improvement on data they can be fully tested. Beyond those sensitivities, the regions that can be explored produce signals that degenerate with standard expectations and so sensitivities are lost. If after enhancing the statistical uncertainty to this value no deviations are observed, neither neutrino decoupling nor BBN observables will be suited tools for testing this hypothesis.

Appendix A: Relevant thermodynamic quantities and collision terms

In this appendix we collect the expressions required to run the network of Boltzmann equations that account for the neutrino decoupling process, Eqs. (12) and (13). We start with standard results for energy density and pressure of relativistic thermal species [64]

$$\rho_\gamma = \frac{\pi^2}{30} g_\gamma T^4, \quad \rho_\nu = \frac{7}{8} \rho_\gamma, \quad (\text{A1})$$

with $g_\gamma = g_\nu = 2$. Pressure follows from these expressions: $p_i = \rho_i/3$ ($i = \gamma, \nu$). At the time of e^+e^- annihilation, electron and positrons undergo a transition from the relativistic to non-relativistic regimes. Energy density as well as pressure has then to be written in the general form [64]

$$\rho_e = \frac{2g_e}{2\pi^2} T^4 \int_{\bar{m}_e}^{\infty} \frac{(x^2 - \bar{m}_e^2)^{1/2}}{e^x + 1} x^2 dx, \quad (\text{A2})$$

$$p_e = \frac{2g_e}{6\pi^2} T^4 \int_{\bar{m}_e}^{\infty} \frac{(x^2 - \bar{m}_e^2)^{3/2}}{e^x + 1} dx, \quad (\text{A3})$$

where the electron chemical potential has been set to zero, $g_e = g_{e^-} = g_{e^+} = 2$ and $\bar{m}_e \equiv m_e/T$. Photon and neutrino temperature partial derivatives follow directly from Eqs. (A1) and are given by $\partial\rho_i/\partial T_i = 4\rho_i/T_i$. For electrons, instead, by

$$\frac{\partial}{\partial T} \rho_e = \frac{2 \cdot 4 g_e}{2\pi^2} T^3 \int_{\bar{m}_e}^{\infty} \frac{(x^2 - \bar{m}_e^2)^{1/2}}{\cosh^2(x/2)} x^3 dx. \quad (\text{A4})$$

$$\lambda_{p \rightarrow n}(q_{\min}, q_{\max}) = \int_{q_{\min}}^{q_{\max}} \sqrt{1 - \frac{m_e}{q+Q}} (q+Q)^2 q^2 f(q+Q, T) [1 - f(q, T_\nu)] dq, \quad (\text{B1})$$

where $Q = m_n - m_p$, $E_e = q + Q$ and $f(x, y) = (e^{x/y} + 1)^{-1}$. Integration limits determine the process for which $\lambda_{p \rightarrow n}$ accounts for. For $p + e \rightarrow \bar{\nu}_e + n$, limits are $q_{\min} = -\infty$ and $q_{\max} = -(m_e + Q)$. For $p + \nu_e \rightarrow \bar{e} + n$, limits read $q_{\min} = 0$ and $q_{\max} = \infty$. In terms of Eq. (B1) the proton reaction rate is then given by

$$\Gamma_{p \rightarrow n} = \frac{\lambda_{p \rightarrow n}(-\infty, -m_e - Q) + \lambda_{p \rightarrow n}(0, \infty)}{m_e^5 \tau_n \lambda_0}, \quad (\text{B2})$$

with the coefficient λ_0 written according to [58]

$$\lambda_0 = \sqrt{\bar{\Delta}^2 - 1} \left(\frac{-8 - 9\bar{\Delta}^2 + 2\bar{\Delta}^4}{60} \right) + \frac{\bar{\Delta}}{4} \text{arcosh}(\bar{\Delta}), \quad (\text{B3})$$

where $\bar{\Delta} \equiv Q/m_e$.

Collision terms follow from electron, positron, neutrino and anti-neutrino electroweak neutral and charged current scattering processes (contributions from s , t and u channels are present) [65]. Assuming a Maxwell-Boltzmann distribution and $T_{\nu_i} \equiv T_\nu$, following Ref. [49] they can be written according to

$$\frac{\delta\rho_{\nu_e}}{\delta t} = \frac{G_F^2}{\pi^5} [(1 + 4\sin^2\theta_W + 8\sin^4\theta_W)F(T, T_\nu)], \quad (\text{A5})$$

$$\frac{\delta\rho_{\nu_\mu}}{\delta t} = \frac{G_F^2}{\pi^5} [(1 - 4\sin^2\theta_W + 8\sin^4\theta_W)F(T, T_\nu)], \quad (\text{A6})$$

with the function F given by [49]

$$F(T_1, T_2) = 32(T_1^9 - T_2^9) + 56T_1^4 T_2^4 (T_1 - T_2). \quad (\text{A7})$$

For the weak mixing angle we have employed $\sin^2\theta_W = 0.223$ [12].

Appendix B: Proton leading-order rate in the infinite mass nucleon limit

The leading-order proton reaction rate $\Gamma_{p \rightarrow n}$ consist of two terms: $\Gamma_{p+e \rightarrow \bar{\nu}_e+n}$ and $\Gamma_{p+\nu_e \rightarrow \bar{e}+n}$. Both can be written in terms of the integral $\lambda_{p \rightarrow n}$ [64, 66]

ACKNOWLEDGMENTS

We warmly thank Nicolás Fernández, Kazunori Kohri and Robert Scherrer for very useful comments on the manuscript. A.V. thanks the Theoretical Astroparticle and Neutrino Physics Group of the University of Torino and INFN for their hospitality. The work of D.A.S. and A.V. is supported by ANID under project number 1221445. S.G. thanks “Universidad Técnica Federico Santa María” in Santiago de Chile for hospitality in the months during which this project was conceived and carried out. S.G. is supported by the European Union’s Framework Programme for Research and Innovation Horizon 2020 (2014–2020) under grant agreement 754496 (FELLINI, until September 2023) and Junior Leader Fellowship LCF/BQ/PI23/11970034 by La Caixa Foundation (from October 2023).

[1] N. Aghanim et al. (Planck), *Astron. Astrophys.* **641**, A6 (2020), [Erratum: *Astron. Astrophys.* 652, C4 (2021)], 1807.06209.

[2] F. Iocco, G. Mangano, G. Miele, O. Pisanti, and P. D. Serpico, *Phys. Rept.* **472**, 1 (2009), 0809.0631.

- [3] M. G. Betti et al. (PTOLEMY), *JCAP* **07**, 047 (2019), 1902.05508.
- [4] M. Punturo et al., *Class. Quant. Grav.* **27**, 194002 (2010).
- [5] K. Yagi and N. Seto, *Phys. Rev. D* **83**, 044011 (2011), [Erratum: *Phys.Rev.D* 95, 109901 (2017)], 1101.3940.
- [6] J. Aasi et al. (LIGO Scientific, VIRGO), *Class. Quant. Grav.* **32**, 115012 (2015), 1410.7764.
- [7] B. P. Abbott et al. (LIGO Scientific), *Class. Quant. Grav.* **34**, 044001 (2017), 1607.08697.
- [8] P. Amaro-Seoane et al. (LISA) (2017), 1702.00786.
- [9] B. D. Fields, K. A. Olive, T.-H. Yeh, and C. Young, *JCAP* **03**, 010 (2020), [Erratum: *JCAP* 11, E02 (2020)], 1912.01132.
- [10] B. D. Fields, K. A. Olive, T.-H. Yeh, and C. Young, *Journal of Cosmology and Astroparticle Physics* **2020**, E02 (2020), URL <https://dx.doi.org/10.1088/1475-7516/2020/11/E02>.
- [11] E. Lisi, S. Sarkar, and F. L. Villante, *Phys. Rev. D* **59**, 123520 (1999), hep-ph/9901404.
- [12] P. D. Group, R. L. Workman, V. D. Burkert, V. Crede, E. Klempt, U. Thoma, L. Tiator, K. Agashe, G. Aielli, B. C. Allanach, et al., *Progress of Theoretical and Experimental Physics* **2022**, 083C01 (2022), ISSN 2050-3911, <https://academic.oup.com/ptep/article-pdf/2022/8/083C01/49175539/ptac097.pdf>, URL <https://doi.org/10.1093/ptep/ptac097>.
- [13] T. Hsyu, R. J. Cooke, J. X. Prochaska, and M. Bolte, *Astrophys. J.* **896**, 77 (2020), 2005.12290.
- [14] C. Giovanetti, M. Lisanti, H. Liu, and J. T. Ruderman, *Phys. Rev. Lett.* **129**, 021302 (2022), 2109.03246.
- [15] T. Hasegawa, N. Hiroshima, K. Kohri, R. S. L. Hansen, T. Tram, and S. Hannestad, *JCAP* **12**, 012 (2019), 1908.10189.
- [16] M. Kawasaki, K. Kohri, and N. Sugiyama, *Phys. Rev. D* **62**, 023506 (2000), astro-ph/0002127.
- [17] M. Kawasaki, K. Kohri, and N. Sugiyama, *Phys. Rev. Lett.* **82**, 4168 (1999), astro-ph/9811437.
- [18] A. Laguë and J. Meyers, *Phys. Rev. D* **101**, 043509 (2020), 1908.05291.
- [19] P. Jordan, *Schwerkraft Und Weltall* (Braunschweig.: F. Vieweg, 1955).
- [20] M. Fierz, *Helv. Phys. Acta* **29**, 128 (1956).
- [21] C. Brans and R. H. Dicke, *Phys. Rev.* **124**, 925 (1961).
- [22] N. Bartolo and M. Pietroni, *Phys. Rev. D* **61**, 023518 (2000), hep-ph/9908521.
- [23] B. Ratra and P. J. E. Peebles, *Phys. Rev. D* **37**, 3406 (1988).
- [24] C. Wetterich, *Nucl. Phys. B* **302**, 668 (1988), 1711.03844.
- [25] J. Khoury, B. A. Ovrut, P. J. Steinhardt, and N. Turok, *Phys. Rev. D* **64**, 123522 (2001), hep-th/0103239.
- [26] J. Khoury, P. J. Steinhardt, and N. Turok, *Phys. Rev. Lett.* **92**, 031302 (2004), hep-th/0307132.
- [27] Y. B. Zeldovich, *Mon. Not. Roy. Astron. Soc.* **160**, 1P (1972).
- [28] P.-H. Chavanis, *Phys. Rev. D* **92**, 103004 (2015), 1412.0743.
- [29] R. J. Scherrer, *Phys. Rev. D* **106**, 103516 (2022), 2209.03421.
- [30] F. D’Eramo, N. Fernandez, and S. Profumo, *JCAP* **05**, 012 (2017), 1703.04793.
- [31] F. D’Eramo, N. Fernandez, and S. Profumo, *JCAP* **02**, 046 (2018), 1712.07453.
- [32] S. Dutta and R. J. Scherrer, *Phys. Rev. D* **82**, 083501 (2010), 1006.4166.
- [33] B. Dutta, C. S. Fong, E. Jimenez, and E. Nardi, *JCAP* **10**, 025 (2018), 1804.07676.
- [34] R. T. Co, D. Dunsy, N. Fernandez, A. Ghalsasi, L. J. Hall, K. Harigaya, and J. Shelton, *JHEP* **09**, 116 (2022), 2108.09299.
- [35] J. D. Barrow and K. Yamamoto, *Phys. Rev. D* **82**, 063516 (2010), 1004.4767.
- [36] J. Lesgourgues and S. Pastor, *Phys. Rept.* **429**, 307 (2006), astro-ph/0603494.
- [37] V. F. Shvartsman, *Pisma Zh. Eksp. Teor. Fiz.* **9**, 315 (1969).
- [38] G. Steigman, D. N. Schramm, and J. E. Gunn, *Phys. Lett. B* **66**, 202 (1977).
- [39] J. J. Bennett, G. Buldgen, M. Drewes, and Y. Y. Y. Wong, *JCAP* **03**, 003 (2020), [Addendum: *JCAP* 03, A01 (2021)], 1911.04504.
- [40] J. J. Bennett, G. Buldgen, P. F. De Salas, M. Drewes, S. Gariazzo, S. Pastor, and Y. Y. Y. Wong, *JCAP* **04**, 073 (2021), 2012.02726.
- [41] J. Froustey, C. Pitrou, and M. C. Volpe, *JCAP* **12**, 015 (2020), 2008.01074.
- [42] J. Froustey and C. Pitrou, *JCAP* **03**, 065 (2022), 2110.11889.
- [43] K. Akita and M. Yamaguchi, *JCAP* **08**, 012 (2020), 2005.07047.
- [44] M. Cielo, M. Escudero, G. Mangano, and O. Pisanti (2023), 2306.05460.
- [45] R. Consiglio, P. F. de Salas, G. Mangano, G. Miele, S. Pastor, and O. Pisanti, *Comput. Phys. Commun.* **233**, 237 (2018), 1712.04378.
- [46] P. Ade et al. (Simons Observatory), *JCAP* **02**, 056 (2019), 1808.07445.
- [47] K. Abazajian et al. (2019), 1907.04473.
- [48] K. N. Abazajian et al. (CMB-S4) (2016), 1610.02743.
- [49] M. Escudero, *JCAP* **02**, 007 (2019), 1812.05605.
- [50] M. Escudero, *JCAP* **05**, 048 (2020), 2001.04466.
- [51] S. Gariazzo, P. F. de Salas, and S. Pastor, *JCAP* **07**, 014 (2019), 1905.11290.
- [52] L. C. Thomas, T. Dezen, E. B. Grohs, and C. T. Kishimoto, *Phys. Rev. D* **101**, 063507 (2020), 1910.14050.
- [53] Y. I. Izotov and T. X. Thuan, *Astrophys. J.* **602**, 200 (2004), astro-ph/0310421.
- [54] Y. I. Izotov and T. X. Thuan, *Astrophys. J.* **665**, 1115 (2007), 0704.3842.
- [55] M. S. Smith, L. H. Kawano, and R. A. Malaney, *Astrophys. J. Suppl.* **85**, 219 (1993).
- [56] O. Pisanti, A. Cirillo, S. Esposito, F. Iocco, G. Mangano, G. Miele, and P. D. Serpico, *Comput. Phys. Commun.* **178**, 956 (2008), 0705.0290.
- [57] S. Gariazzo, P. F. de Salas, O. Pisanti, and R. Consiglio, *Comput. Phys. Commun.* **271**, 108205 (2022), 2103.05027.
- [58] C. Pitrou, A. Coc, J.-P. Uzan, and E. Vangioni, *Phys. Rept.* **754**, 1 (2018), 1801.08023.
- [59] C. Pitrou, A. Coc, J.-P. Uzan, and E. Vangioni, *Mon. Not. Roy. Astron. Soc.* **502**, 2474 (2021), 2011.11320.
- [60] E. Grohs and G. M. Fuller, *Nucl. Phys. B* **911**, 955 (2016), 1607.02797.
- [61] A. T. Yue, M. S. Dewey, D. M. Gilliam, G. L. Greene, A. B. Laptev, J. S. Nico, W. M. Snow, and F. E. Wietfeldt, *Phys. Rev. Lett.* **111**, 222501 (2013), 1309.2623.
- [62] R. W. Pattie, Jr. et al., *Science* **360**, 627 (2018), 1707.01817.
- [63] T. Chowdhury and S. Ipek (2022), 2210.12031.
- [64] R. A. Alpher, J. W. Follin, and R. C. Herman, *Phys. Rev.* **92**, 1347 (1953).
- [65] A. D. Dolgov, *Phys. Rept.* **370**, 333 (2002), hep-ph/0202122.
- [66] S. Weinberg, *Cosmology* (Cambridge University Press, 2008), ISBN 978-0-19-852682-7.